JACS
JOURNAL OF THE AMERICAN CHEMICAL SOCIETY
pubs.acs.org/JACS
Article

A Double Open-Shelled Au_{43} Nanocluster with Increased Catalytic Activity and Stability

Yingwei Li,[§] Hong Ki Kim,[§] Ryan D. McGillicuddy,[§] Shao-Liang Zheng, Kevin J. Anderton, Grant J. Stec, Jaehyeong Lee, Dongtao Cui, and Jarad A. Mason*

Cite This: https://doi.org/10.1021/jacs.3c02458
Read Online
ACCESS | Metrics & More | Article Recommendations | Supporting Information

ABSTRACT: Atomically precise metal nanoclusters (NCs) are an intriguing class of crystalline solids with unique physicochemical properties derived from tunable structures and compositions. Most atomically precise NCs require closed-shells and coordinatively saturated surface metals in order to be stable. Herein, we report $Au_{43}(C{\equiv}C^tBu)_{20}$ and $Au_{42}Ag_1(C{\equiv}C^tBu)_{20}$, which feature open electronic and geometric shells, leading to both paramagnetism (23 valence e^-) and enhanced catalytic activity from a single coordinatively unsaturated surface metal. The Au-alkynyl surface motifs of these NCs form five helical stripes around the inner Au_{12} kernel, imparting chirality and high thermal stability. Density functional theory (DFT) calculations suggest that there are minimal energy differences between the open-shelled NCs and hypothetical closed-shell systems and that the open-shelled electronic configuration gives rise to the largest band gap, which is known to promote cluster stability. Furthermore, we highlight how coordinatively unsaturated surface metals create active sites for the catalytic oxidation of benzyl alcohol to benzaldehyde, leading to high selectivity and increased conversion. This work represents the first example of an atomically precise Au NC with a double open-shelled structure and provides a promising platform for investigating the magnetic and catalytic properties of noble metal nanoparticles.

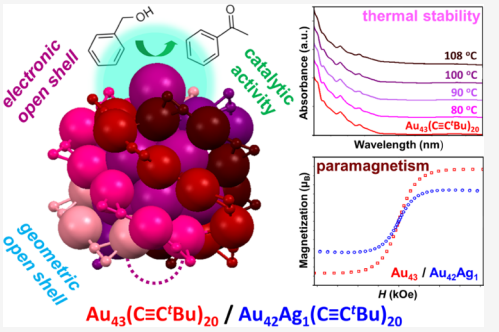

INTRODUCTION

Supported metal nanoparticles are widely used as heterogeneous catalysts due to their high activity and unique selectivity for a variety of chemical transformations.[1,2] In general, catalyst performance can be tailored by manipulating the size, shape, and surface structure of the nanoparticles,[3,4] with activity and selectivity towards different products influenced by the surface area to volume ratio and by the specific microenvironment around active metal sites located on the nanoparticle surface.[5,6] It is, however, difficult to obtain molecular-level insights into how nanoparticle structure and composition affects catalytic properties because of the heterogeneity of typical nanoparticle catalysts, which leads to a wide distribution of active sites that are challenging to identify and study experimentally. This is in contrast to single-atom and molecular catalysts for which structure-property relationships can be much more readily and rigorously established.[7−12]

Recently, atomically precise metal nanoclusters (NCs) with a core size of ∼1−2 nm have emerged as a new class of catalysts that bridge a gap between conventional nanoparticle and molecular catalysts.[13,14] Owing to their homogeneity, crystallography can be used to determine the complete structures (metal core and ligand shell) of atomically precise NCs, allowing atomic structure to be correlated directly to different physicochemical properties, including catalytic performance.[15,16] Indeed, systematically altering the size,[17,18] structure,[19−21] composition,[22] and surface ligands[23,24] of atomically precise NCs has provided mechanistic insights into many important catalytic reactions, including hydrogenation,[25] CO oxidation,[26,27] the hydrogen evolution reaction,[15,28] and electrocatalytic CO_2 reduction.[29,30]

Owing to their high surface energy, the chemical and thermal stability of atomically precise NCs often limits the range of reaction conditions that can be explored for catalysis, particularly when coordinatively unsaturated metal centers (open metal sites) are present. In addition, a closed-shell electronic configuration is preferred for clusters of group 11 elements,[31] and superatom theory[32−34] and electron-counting rules[35,36] have been developed to explain cluster stability. As such, paramagnetic NCs with one unpaired electron (electronic open-shell) typically adopt a symmetric structure (commonly spherical or spheroidal) fully passivated by a dense ligand shell in order to be stable.[37−39] For example, the NC $Au_{99}(C{\equiv}CR)_{40}$ has a single unpaired electron and exhibits D_5 symmetry.[40] In addition, a carboranealkynyl-protected Au_{28}

Received: March 7, 2023

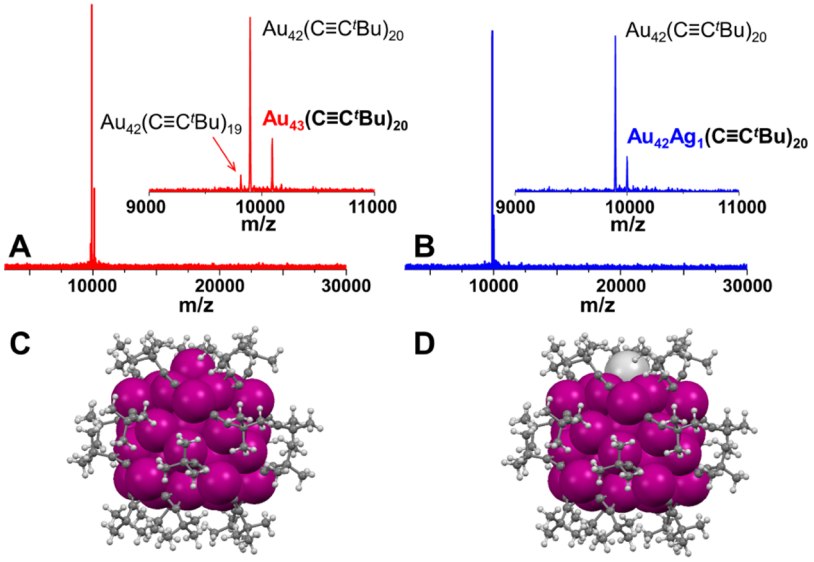

Figure 1. MALDI-MS spectra and the crystal structures of (A, C) $Au_{43}(C{\equiv}C^tBu)_{20}$ and (B, D) $Au_{42}Ag_1(C{\equiv}C^tBu)_{20}$ NCs. Large magenta, large light grey, dark grey, and white spheres represent Au, Ag, C, and H atoms, respectively.

NC with 13 valence electrons rapidly transforms into a more stable and symmetric Au_{23} NC with 12 valence e^-.[41]

In addition to favoring diamagnetic atomically precise NCs with closed-shell electronic configurations, the requirements for NC stability are often incompatible with the existence of coordinatively unsaturated metal centers, which serve as catalytically active sites with tunable and predictable electronic structures and steric environments.[42] For conventional nanoparticle catalysts, coordinatively unsaturated metal sites are usually formed during a thermal activation process to remove some fraction of bound surface ligands.[43] Though this can lead to high catalytic activity, there is limited ability to control the specific microenvironment around the resulting coordinatively unsaturated metal sites, and there is typically a wide distribution of local microenvironments. Atomically precise nanochemistry provides a platform for targeting unligated surface metal atoms in a much more controlled fashion to serve as active catalytic sites. Moreover, there have not been any reports of atomically precise metal NCs that exhibit both geometric and electronic open-shelled structures, which might provide access to unique combinations of magnetic and catalytic properties.

Herein, we report the first example of such a double open-shelled NC. Specifically, we describe the synthesis and detailed characterization of $Au_{43}(C{\equiv}C^tBu)_{20}$, which—despite having a classic $Au_{12}@Au_{20}$ kernel structure—only contains 11 Au atoms around the kernel, resulting in an atomic vacancy (geometric open-shell) and a single unpaired valence electron (electronic open-shell). Importantly, 10 of the surface Au atoms are stabilized by 20 alkynyl ligands arranged in five helical stripes on the kernel that leave a single Au atom unligated. The NC features high thermal stability, and the unligated Au atom can be controllably replaced by Ag during the NC synthesis to form $Au_{42}Ag_1(C{\equiv}C^tBu)_{20}$, providing a model system to study the effect of a single-atom substitution on catalytic reactivity. Compared to other alkynyl- or thiolate-protected NCs without coordinatively unsaturated metal sites, $Au_{43}(C{\equiv}C^tBu)_{20}$ exhibits higher activity and selectivity for the oxidation of benzyl alcohols to benzaldehydes.

RESULTS AND DISCUSSION

Synthesis and Characterization of Double Open-Shelled NCs. Alkynyl-protected Au NCs have received increasing attention because of the unique coordination modes that alkynyl ligands can adopt on Au surfaces.[44−48] Since magic-numbered Au-alkynyl NCs typically have smaller ligand-to-Au ratios than their Au-thiolate counterparts,[49,50] it should be easier to promote the formation of coordinatively unsaturated metal sites for catalysis, though this has not yet been demonstrated for existing Au-alkynyl NCs. In pursuit of a stable Au-alkynyl NC bearing at least one coordinatively unsaturated surface metal site, we selected $HC{\equiv}C^tBu$ as a surface ligand since it has a small footprint area but contains a sterically bulky head group, which could lead to more accessibility for substrates during catalysis. The new atomically precise $Au_{43}(C{\equiv}C^tBu)_{20}$ (**Au_{43}**) NC was synthesized by first reducing an oligomeric $Au^I{-}C{\equiv}C^tBu$ precursor with borane *tert*-butylamine in the presence of triethylamine. The reaction was allowed to proceed overnight, and after washing with methanol, the resulting mixture of Au NCs was separated by preparative thin layer chromatography (see Supporting Information for details). Different bands were identified according to their colors (Figure S1). The first brown band corresponded to **Au_{43}**, while the second and third bands were determined to be two previously reported $Au_{23}(C{\equiv}C^tBu)_{15}$ isomers by ultraviolet−visible (UV−vis) spectroscopy and matrix assisted laser desorption ionization mass spectrometry (MALDI-MS, Figure S2).[51]

The **Au_{43}** NCs exhibit sharp absorption peaks in the UV−vis-NIR spectrum at 360, 460, and 570 nm, as well as a broad absorption band centered at 1125 nm (Figure S3, red line). MALDI-MS confirms the presence of $Au_{43}(C{\equiv}C^tBu)_{20}$ and also contains two other fragment peaks that can be assigned to $Au_{42}(C{\equiv}C^tBu)_{20}$ and $Au_{42}(C{\equiv}C^tBu)_{19}$ (Figure 1A). Note that Tsukuda et al. observed phenylacetylene-protected Au_{43} NCs via MS a decade ago,[49] but their precise formula—and structure—was not determined. Moreover, compared to the 25 thiolate ligands that protect Au_{43} clusters such as $Au_{43}(S\text{-}c\text{-}C_6H_{11})_{25}$,[52] the 20 surface ligands surrounding

https://doi.org/10.1021/jacs.3c02458
J. Am. Chem. Soc. XXXX, XXX, XXX−XXX

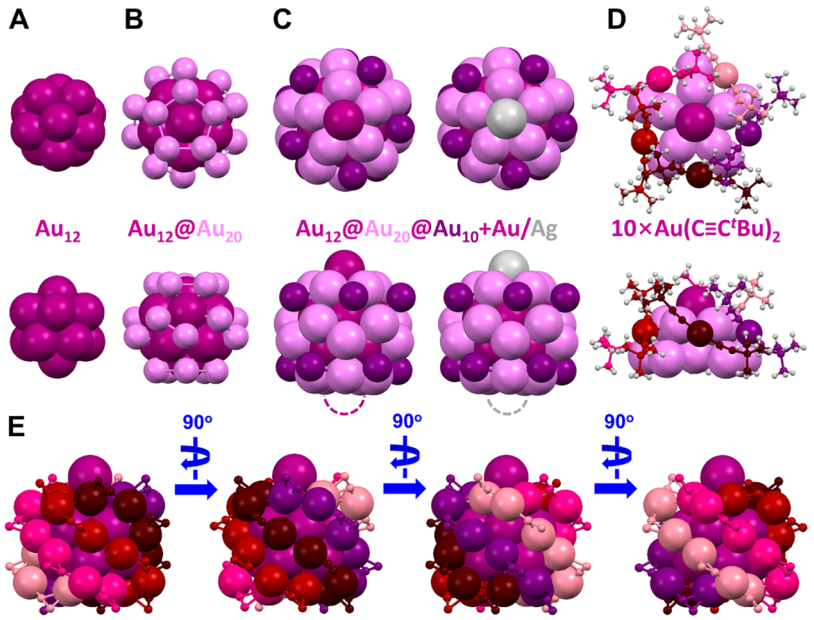

Figure 2. Structures of $Au_{43}(C{\equiv}C^tBu)_{20}$ and $Au_{42}Ag_1(C{\equiv}C^tBu)_{20}$ NCs shown from a top view (upper) and side view (lower) illustrating the (A) icosahedral Au_{12} inner kernel, (B) dodecahedral Au_{20} shell, (C) 10 capping Au atoms and one coordinatively unsaturated Au or Ag atom on the Au_{20} shell with the vacancy highlighted by the dashed circle, and (D) five linear ^{t}BuC≡C−Au−C≡C^{t}Bu motifs on the top (five motifs at the bottom not shown). (E) Five helical $Au_6(C{\equiv}C^tBu)_4$ stripes wrapping the Au_{12} kernel along a C_5 axis. For (A, C), magenta, violet, and purple spheres represent Au atoms, and light grey spheres represent Ag atom; while in (D), the five ^{t}BuC≡C−Au−C≡C^{t}Bu motifs are shown in different colors, and in (E), the five helical stripes are marked in different colors, and the ^{t}Bu groups are omitted for clarity.

$Au_{43}(C{\equiv}C^tBu)_{20}$ demonstrate how alkynyl ligands can lead to smaller ligand-to-Au ratios.

Plate-shaped **Au_{43}** single crystals suitable for single-crystal X-ray diffraction (SC-XRD) were obtained via a layer-diffusion method. The crystal structure of **Au_{43}** contains disordered surface Au atoms with bound alkynyl ligands (Figure 1C, and Table S1). Similar surface disorder has also been observed for other Au-alkynyl NCs, including $Au_{144}(C{\equiv}CR)_{60}$.[53] Since heteroatom doping can affect the symmetry of NCs and their crystallization behavior,[20] we hypothesized that a NC of the form $Au_{43-x}Ag_x$ might be accessible that was isostructural to **Au_{43}** but with reduced surface disorder. By adding a small amount of Ag(I) (molar ratio Au/Ag = 20:1) prior to reduction, we were able to obtain $Au_{42}Ag_1(C{\equiv}C^tBu)_{20}$ (**$Au_{42}Ag_1$**) (Figure 1B), which features a nearly identical crystal structure to **Au_{43}** and substantially more ordered surface metal atoms and ligands (Figure 1D, and Table S2). As a result, the two NCs crystallize in different space groups—*Cmca* for **Au_{43}** and *Pbca* for **$Au_{42}Ag_1$**.

Both 43-metal NCs have an icosahedral Au_{12} inner kernel surrounded by a dodecahedral Au_{20} shell (Figure 2A,B). Interestingly, only 11 of the 12 facets of the Au_{20} shell are capped by metal atoms, leaving a vacant site on each NC (Figure 2C). For **$Au_{42}Ag_1$**, crystallography reveals that the vacant site is always directly opposite the Ag atom, and the Ag atom and vacancy are disordered with equal probability at each site. The presence of Ag on the surface of the cluster—rather than within the kernel—is consistent with the absorption spectrum of **$Au_{42}Ag_1$**, which matches that of **Au_{43}** (Figure S3, blue line).[54] The same substitutional disorder between an unligated surface metal site and vacancy is present in **Au_{43}**, and similar 50% occupancy at opposite sites was also recently observed for a Au_{55} NC co-protected by thiolate and phosphine surface ligands.[55] We note that the crystal structure of **$Au_{42}Ag_1$**—along with MS data—rules out the possibility that **Au_{43}** is actually a 1:1 co-crystal of $Au_{42}(C{\equiv}C^tBu)_{20}$ and $Au_{44}(C{\equiv}C^tBu)_{20}$.

In **Au_{43}** and **$Au_{42}Ag_1$**, the 20 alkynyl ligands are directly bound to 10 Au surface atoms through terminal σ-bonds and have additional π interactions with a nearby Au atom from the inner Au_{20} shell (Figure 2D). Consequently, five sets of linear ^{t}BuC≡C−Au−C≡C^{t}Bu motifs encircle the apical metal site, which is coordinatively unsaturated and does not interact with any of the alkyny ligands (Figure 2D, top). The combination of σ- and π-bonding motifs leads to five helical $Au_6(C{\equiv}C^tBu)_4$ stripes (i.e., Au−C≡C−Au−C≡C−Au−Au−C≡C−Au−C≡C−Au) that wrap the icosahedral Au_{12} kernel along the central C_5 axis (Figure 2E, marked in different colors). The five helical stripes extend from one pole to the other in a clockwise or anticlockwise fashion, making **Au_{43}** and **$Au_{42}Ag_1$** chiral NCs (both enantiomers are present in the crystal, Figure S6).[56] Though such a helical surface pattern has been observed for thiolate- and phosphine-protected Au NCs previously,[37,57] this represents, to the best of our knowledge, the first time it has been observed for Au/alkynyl NCs. Indeed, the alkynyl surface ligands on two superatomic $Au_{24}Ag_{20}$ NCs (alkynyl = C≡CPh or C≡CPh^{t}Bu) do not adopt a helical arrangement or any type of ordered pattern (Figure S7).[58,59]

Electrospray ionization mass spectroscopy (ESI-MS) was used to confirm the assigned stoichiometry of the NCs. However, no peak for neat **Au_{43}** or **$Au_{42}Ag_1$** NCs was observed. This is likely because the neutral NCs either lose one Au or Ag atom, or pick up one Au atom along with an alkynyl ligand, in order to be ionized (Figures S4 and S5).[60,61] The observed isotopic patterns (red/blue lines) match well with the calculated ones (black lines), and the +1 and +2 charges are due to the ionization, not the native charge states of the NCs. We suspect that the double open-shelled nature of the **Au_{43}** and **$Au_{42}Ag_1$** NCs makes it difficult to get clean MS spectra,[49]

https://doi.org/10.1021/jacs.3c02458
J. Am. Chem. Soc. XXXX, XXX, XXX−XXX

making crystallography the most reliable method to determine their composition.

The vacant atomic site (indicated by the dashed circle in Figure 2C) in both $\mathbf{Au_{43}}$ and $\mathbf{Au_{42}Ag_1}$ is surprising given the precedent for 44-metal NCs, including two $Au_{24}Ag_{20}$ NCs and one $Au_{22}Ag_{22}$ NC, which all contain complete shells of surface metals and closed electronic shells.[58,59,62] Moreover, the previously reported 43-metal NC, $PtAg_{42}(C{\equiv}CR)_{28}$, has a closed-shell Ag_{30} cage surrounding a $Pt@Ag_{12}$ kernel.[63] In addition to their open surface shells, $\mathbf{Au_{43}}$ and $\mathbf{Au_{42}Ag_1}$ possess an open-shell electronic configuration (23 valence electrons) with a single unpaired e^-, which is rare and typically leads to poor stability.

Stability of 43-Metal NCs. To evaluate how the coordinatively unsaturated site and open-shell electronic configuration impact the thermal stability of $\mathbf{Au_{43}}$ and $\mathbf{Au_{42}Ag_1}$, we heated dispersions of each NC in toluene at elevated temperatures for up to 7 days and monitored the integrity of the cluster by UV−vis spectroscopy. As shown in Figure 3A, both NCs feature exceptional thermal stability, with

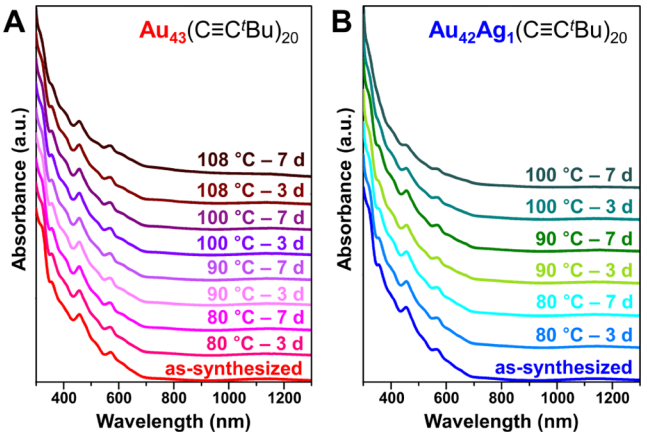

Figure 3. UV−vis-NIR spectra of (A) $\mathbf{Au_{43}}$ and (B) $\mathbf{Au_{42}Ag_1}$ NCs held at different temperatures for 3 or 7 days.

no changes observed to the $\mathbf{Au_{43}}$ spectrum even after heating at 108 °C—just below the solvent boiling point—for 7 days. Although $\mathbf{Au_{42}Ag_1}$ NCs are less stable than their pure gold counterparts, no degradation was observed while holding at 90 °C for 7 days, and the UV−vis peak intensities only began to decrease after holding at 100 °C for more than 3 days (Figure 3B). By contrast, $Au_{23}(C{\equiv}C^tBu)_{15}$ changes to another isomer within 9 h at ambient temperature,[51] and $Au_{25}(SR)_{18}^-$ (R = C_2H_4Ph) degrades within 1 day when heated in toluene at 60 °C.[64]

To gain additional insight into the stability of $\mathbf{Au_{43}}$ and $\mathbf{Au_{42}Ag_1}$, we performed density functional theory (DFT) calculations for the NCs, along with hypothetical closed-shell $Au_{42}(C{\equiv}C^tBu)_{20}$, $Au_{44}(C{\equiv}C^tBu)_{20}$, and $Au_{42}Ag_2(C{\equiv}C^tBu)_{20}$ NCs that were constructed by adding one atom to the unoccupied surface site or removing the coordinatively unsaturated surface metal atom of the corresponding 43-metal cluster. The relative electronic energies (ΔE) were estimated by the following equations

$$\Delta E(\mathbf{Au_{43}}) = E(\mathbf{Au_{43}}) - [E(Au_{42}) + E(Au_{44})]/2 \quad (1)$$

$$\Delta E(\mathbf{Au_{42}Ag_1}) = E(\mathbf{Au_{42}Ag_1}) - [E(Au_{42}) + E(Au_{42}Ag_2)]/2 \quad (2)$$

Surprisingly, $\Delta E(\mathbf{Au_{43}})$ and $\Delta E(\mathbf{Au_{42}Ag_1})$ are 0.276 and −0.527 kcal/mol, respectively, which are both within the range of the expected error of the DFT calculations (Table S3). These results indicate that there are minimal energy differences between the 42-, 43-, and 44-metal NCs and confirm the feasibility of $\mathbf{Au_{43}}$ and $\mathbf{Au_{42}Ag_1}$. Moreover, we hypothesize that the stability of the double open-shelled $\mathbf{Au_{43}}$ and $\mathbf{Au_{42}Ag_1}$ NCs can be attributed, in part, to the helical arrangement of surface ligands reducing surface energy in a manner that is similar to how helix conformations are preferentially adopted by many nanostructures, including ZnO nanobelts[65] and Al, Au, and PdSe nanowires.[66−68]

The optical band gaps of $\mathbf{Au_{43}}$ and $\mathbf{Au_{42}Ag_1}$ were experimentally determined to be ∼0.78 eV (Figure 4A). The frontier molecular orbitals (FMOs) of the experimental and hypothetical NCs were calculated by DFT. The singly occupied molecular orbital (SOMO) and the lowest unoccupied molecular orbitals (LUMO) of $\mathbf{Au_{43}}$ are delocalized across the entire Au core (Figure 4B), while the SOMO of $\mathbf{Au_{42}Ag_1}$ is more localized on the coordinatively unsaturated Ag site (Figure 4C). The calculated SOMO−LUMO energy gaps of $\mathbf{Au_{43}}$ and $\mathbf{Au_{42}Ag_1}$ NCs are 0.71 and 0.74 eV, respectively (Figure 4B,C), which is consistent with

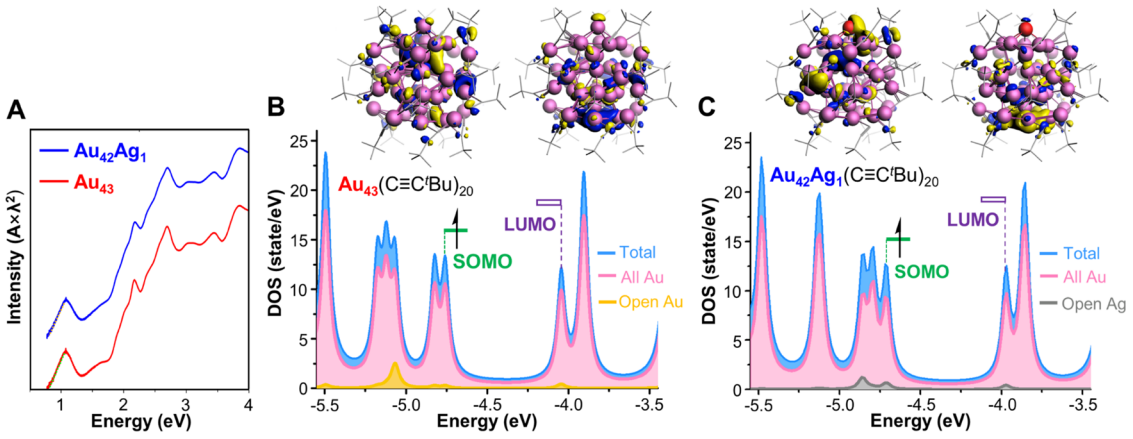

Figure 4. (A) UV−vis-NIR absorption spectra (photon energy scale) of $Au_{43}(C{\equiv}C^tBu)_{20}$ and $Au_{42}Ag_1(C{\equiv}C^tBu)_{20}$ in toluene are shown (spectra are offset vertically for clarity). Isosurface plots (isodensity value = 0.02 a.u.) of SOMO and LUMO and density of states with their corresponding energy levels for the experimental (B) $Au_{43}(C{\equiv}C^tBu)_{20}$ and (C) $Au_{42}Ag_1(C{\equiv}C^tBu)_{20}$.

https://doi.org/10.1021/jacs.3c02458
J. Am. Chem. Soc. XXXX, XXX, XXX−XXX

the experimental band gaps. In other frontier MOs, strong localization on the open Au or Ag sites is only found in the HOMO − 2 (HOMO − 2 = 3rd highest-energy occupied molecular orbital) (Figures S8 and S9).

In contrast, the hypothetical $Au_{42}(C{\equiv}C^tBu)_{20}$ has a smaller energy gap of 0.65 eV, and no distinct localization was found in any frontier MOs (Figure S10). Furthermore, the energy gaps of the hypothetical closed-shell $Au_{44}(C{\equiv}C^tBu)_{20}$ and $Au_{42}Ag_2(C{\equiv}C^tBu)_{20}$ NCs were 0.14 and 0.06 eV, respectively (Figures S11 and S12), which are much smaller than the band gaps of $\mathbf{Au_{43}}$ and $\mathbf{Au_{42}Ag_1}$. This result further underpins why 44-metal NCs were not observed during NC synthesis (Figure 1A,B).

Magnetic Properties of 43-Metal NCs. With 23 valence electrons and a single unpaired electron, both $\mathbf{Au_{43}}$ and $\mathbf{Au_{42}Ag_1}$ should be paramagnetic.[69] To investigate the magnetic properties of the NCs, we first employed electron paramagnetic resonance (EPR) spectroscopy. The X-band spectra of $\mathbf{Au_{43}}$ and $\mathbf{Au_{42}Ag_1}$ dissolved in chloroform (~0.5 mM) display a very weak EPR signal at 4.5 K that is consistent with the presence of an unpaired electron (Figure S13). Interestingly, $\mathbf{Au_{43}}$ showed a branched signal in the g-tensor (Figure S13, red line) that is similar to the well-studied $Au_{25}(SR)_{18}$ (SR = thiolate), which is also a paramagnetic cluster with a single unpaired valence electron.[38,70,71] Because of the low intensity of the EPR signal, however, we cannot fully exclude the possibility that this signal arises from background O_2 dissolved in chloroform.

To more directly characterize the magnetic properties of the NCs in the solid state, we employed superconducting quantum interference device (SQUID) measurements.[71] Although the saturation magnetization is less than the theoretical value expected for one unpaired electron in the ground state (1 μB for $g = 2$), typical paramagnetic behavior was observed for both $\mathbf{Au_{43}}$ and $\mathbf{Au_{42}Ag_1}$ NCs at 2 K with no hysteresis (Figure 5). A

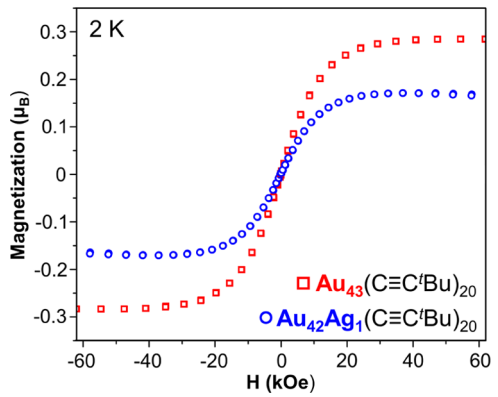

Figure 5. Magnetization (μ_B) of $Au_{43}(C{\equiv}C^tBu)_{20}$ and $Au_{42}Ag_1(C{\equiv}C^tBu)_{20}$ plotted as a function of magnetic field (kOe) at 2 K.

lower than expected saturation magnetization has also been reported for $Au_{99}(C{\equiv}CR)_{40}$.[40] The lower saturation magnetization of Au-alkynyl NCs could be attributed to antiferromagnetic coupling between the NCs. The $\mathbf{Au_{42}Ag_1}$ NCs show even lower saturation magnetization than $\mathbf{Au_{43}}$, which is consistent with EPR measurements. The lower magnetization of the $\mathbf{Au_{42}Ag_1}$ NC can be attributed to a more localized SOMO on the single Ag atom (different distribution of spin density), as indicated in Figure 4C, and the difference in spin−orbit coupling between Au and Ag.[72] The different charge density between Ag and Au on the 43-metal NCs might also affect the antiferromagnetic coupling. Overall, the magnetic properties—coupled with crystallographic and MS data—are consistent with $\mathbf{Au_{43}}$ and $\mathbf{Au_{42}Ag_1}$ NCs having open-shell electronic configurations.

Catalytic Properties of the 43-Metal NCs. Given the presence of a single coordinatively unsaturated site at the apical position of $\mathbf{Au_{43}}$ (Figure 2D), we anticipated that this NC might exhibit higher activity for certain catalytic reactions than similarly sized clusters protected by a dense ligand shell. Surface ligands have a double-edged effect on catalysis——preventing rearrangement of the NCs but also blocking access of the substrate to reactive metal centers.[26] Previously, thiolate- or phosphine-protected NCs have been activated on solid supports by calcination (200 to 500 °C) to remove surface ligands prior to oxidative catalysis.[73−75] Although aggregation can be prevented at low NC loadings, structural rearrangement is inevitable upon complete ligand removal.[76] The use of milder oxidants during catalysis, such as H_2O_2 or *tert*-butyl hydroperoxide (TBHP), can minimize ligand removal and NC rearrangement.[77−80] Recently, Au_{23} NCs co-protected by bulky phosphine and planar dipyridyl amine ligands, which contain 8 open surface metal sites, were shown to have excellent performance for the selective oxidation of benzyl alcohol.[81]

To evaluate how the single coordinatively unsaturated site of $\mathbf{Au_{43}}$ influences its reactivity, we similarly selected benzyl alcohol oxidation as a model reaction. Specifically, $\mathbf{Au_{43}}$ was loaded on an Al_2O_3 support to prepare $\mathbf{Au_{43}}/Al_2O_3$ catalysts. The NC structure was maintained during the catalytic reaction, as we were able to extract a small amount of NCs from the support that did not exhibit any significant changes to their UV−vis spectra after 2 h of catalysis (Figure S14A,B). Further, scanning transmission electron microscopy (STEM) images show that the NCs are homogeneously distributed on the support after the catalytic reaction (Figure S14C,D). Longer reaction times (6 or 24 h), however, made it difficult to recycle the NCs, which could probably be attributed to partial—or complete—ligand removal.

The conversion and selectivity for ketone over ester products were determined by ^{1}H NMR analysis (Table 1, and Figures S15−S29). The $\mathbf{Au_{43}}/Al_2O_3$ catalysts showed a 32% conversion and 98% selectivity after 2 h. Based on the assumption that the apical Au atom represents the only active site, a turnover frequency (TOF) for the $\mathbf{Au_{43}}/Al_2O_3$ catalyst of 0.43 s^{-1} can be calculated. When the reaction time was increased from 6 to 24 h, the TOF dropped to 0.23 s^{-1} with 52% conversion and 0.077 s^{-1} with 68% conversion, respectively, which could be attributed to the depletion of oxidant or the loss of ligands.

The importance of the coordinatively unsaturated Au site on $\mathbf{Au_{43}}$ for catalysis is highlighted in three ways. First, other Au/alkynyl NCs without any open metal sites, including $Au_{23}(C{\equiv}C^tBu)_{15}$ with the same ligands ($\mathbf{Au_{23}}$, Figure S2, green line),[53] and $Au_{44}(C{\equiv}CPh)_{28}$ with a similar size to $\mathbf{Au_{43}}$ ($\mathbf{Au_{44}}$, Figure S30A),[44] have substantially lower conversions under the same reaction conditions. Second, since the apical atom can be either Au or Ag, we can evaluate how the identity of the metal site impacts catalysis. Though Au and Ag might be expected to be equally active for benzyl alcohol oxidation, the conversion of $\mathbf{Au_{42}Ag_1}/Al_2O_3$ is only 7% at 2 h and 18% at 6 h, respectively (entry 7/8). This substantial change upon a single atom substitution is consistent with the majority of catalysis happening at the open metal site. To further explain this effect,

https://doi.org/10.1021/jacs.3c02458
J. Am. Chem. Soc. XXXX, XXX, XXX−XXX

Table 1. Catalytic Performance for Different Au NC/Al_2O_3 Catalysts for Benzyl Alcohol Oxidation[a]

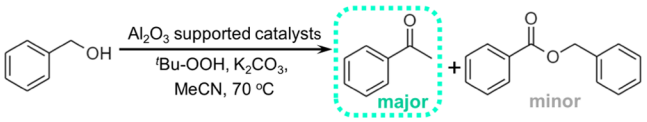

entry	catalyst	reaction time (h)	conversion (%)	selectivity (%)
1	Au_{43}/Al_2O_3	2	32	98
2	Au_{43}/Al_2O_3	6	52	96
3	Au_{23}/Al_2O_3	2	5	100
4	Au_{23}/Al_2O_3	6	8	100
5	Au_{44}/Al_2O_3	2	8	100
6	Au_{44}/Al_2O_3	6	16	100
7	$Au_{42}Ag_1/Al_2O_3$	2	7	100
8	$Au_{42}Ag_1/Al_2O_3$	6	18	100
9	Au_{43}/Al_2O_3*	2	5	100
10	Au_{43}/Al_2O_3*	6	13	100
11	Au_{44}-S/Al_2O_3	2	1	100
12	Au_{44}-S/Al_2O_3	6	4	100
13	Au_{24}-S/Al_2O_3	2	2	100
14	Au_{24}-S/Al_2O_3	6	4	100
15	Al_2O_3	6	n.r.	-

[a]Reaction conditions: 20 mg Al_2O_3-supported catalyst (1 wt % loading of a given NC); $PhCH_2OH$, 20 μL; K_2CO_3, 8 mg; TBHP (^{t}Bu−OOH), 20 μL (70% aqueous solution); acetonitrile, 4 mL. The conversion and selectivity were determined by ^{1}H NMR. n.r. = no reaction. *4-^{t}Bu-$PhCH_2OH$ instead of $PhCH_2OH$.

topographic steric hindrance maps were employed to analyze the pocket around the open metal sites on $\mathbf{Au_{43}}$ and $\mathbf{Au_{42}Ag_1}$ NCs.[82,83] Despite the close similarity of the two 43-metal NCs, the bond length between the apical Ag atom and the nearest Au atom is 2.583(8) Å for $\mathbf{Au_{42}Ag_1}$, while the corresponding Au−Au bond length in $\mathbf{Au_{43}}$ is 2.935(4) Å. The ∼13% difference in the bond length leads to a smaller buried volume (%V_{bur}) for the open Au atom (61.8%) than for the open Ag atom (63.6%) (Figure 6A). As such, the topographical analysis suggests that the coordinatively unsaturated Au atom is a more "open" catalytic site than the Ag atom.

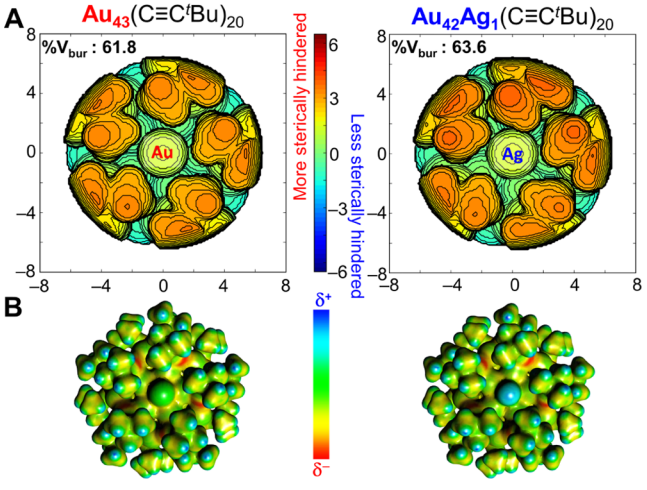

Figure 6. (A) Topographic steric hindrance maps and (B) electrostatic potential maps of (left) $Au_{43}(C{\equiv}C^tBu)_{20}$ and (right) $Au_{42}Ag_1(C{\equiv}C^tBu)_{20}$.

In addition to steric considerations, the rate-determining step of benzyl alcohol oxidation involves hydride transfer from the benzylic carbon to a metal atom.[84,85] As H has a smaller electronegativity (2.20) than Au (2.54) but larger than Ag (1.93), a hydride will behave differently when attached to Au (H as a metal)[86,87] compared to Ag (H as a ligand) on a NC.[88,89] Moreover, the single Ag bears a partial positive charge while the single Au is neutral, as indicated by a calculated electrostatic potential map (Figure 6B). We expect that both steric and electronic factors contribute to the lower activity of $\mathbf{Au_{42}Ag_1}/Al_2O_3$ catalysts compared to $\mathbf{Au_{43}}/Al_2O_3$.

Third, the role of the coordinatively unsaturated metal site was further examined using 4-*tert*-burtyl benzyl alcohol as a representative sterically bulky substrate for which diffusion into the catalytic pocket would be hindered. As expected, the catalytic performance of $\mathbf{Au_{43}}/Al_2O_3$ decreased substantially (entry 9/10). This is consistent with previous reports of lower conversion for supported Au NPs as the distance between the open site and substrate increases.[85] In addition, the effect of surface ligands was also studied by using Au-thiolate NCs of similar sizes, including $Au_{44}(SPh^tBu)_{28}$ ($\mathbf{Au_{44}}$**−S**, Figure S30B)[90] and $Au_{24}(SCH_2Ph)_{20}$ ($\mathbf{Au_{24}}$**−S**, Figure S30C) without coordinatively unsaturated metal sites.[91] From the experimentally determined conversions for $\mathbf{Au_{44}}$**−S**/Al_2O_3 (entry 11/12) and $\mathbf{Au_{24}}$**−S**/Al_2O_3 (entry 13/14) catalysts, it is clear that both Au-thiolate NCs are not as active as the Au-alkynyl ones for benzyl alcohol oxidation, at least under the mild catalytic conditions used here. Collectively, these results underpin that the accessibility of the single open site on Au_{43} NCs is critical to its catalytic performance.

CONCLUSIONS

In summary, $Au_{43}(C{\equiv}C^tBu)_{20}$ represents the first example of an atomically precise Au NC with both an open-shell electronic configuration and open-shell geometric structure containing a coordinatively unsaturated metal site. The $\mathbf{Au_{43}}$ NC has an Au_{12}@Au_{20} kernel, and 11 out of the 12 facets of the cuboctahedra Au_{20} shell are capped with Au atoms. Surface Au atoms are covered by alkynyl ligands that form five helical $Au_6(C{\equiv}C^tBu)_4$ stripes wrapping the kernel, leaving one surface gold uncoordinated to any ligand. The open Au atom can be substituted for Ag to form an isostructural NC with a single coordinatively unsaturated heteroatom. The double open-shelled 43-metal NCs feature high thermal stability, and DFT calculations suggest these NCs have similar energies as hypothetical closed-shell Au_{42}, Au_{44}, and $Au_{42}Ag_2$ NCs. The open-shell electronic configuration of $\mathbf{Au_{43}}$ and $\mathbf{Au_{42}Ag_1}$ was confirmed by SQUID and EPR measurements, and the coordinatively unsaturated Au site was found to lead to higher catalytic activity for benzyl alcohol oxidation than similar NCs with no open metal sites. Further, the helical surface pattern of the 43-metal NCs opens up new opportunities for designing highly stable NCs with open-shelled structures and interesting magnetic and catalytic properties.

ASSOCIATED CONTENT

Supporting Information

The Supporting Information is available free of charge at https://pubs.acs.org/doi/10.1021/jacs.3c02458.

Additional experimental details; X-ray crystallography data; ESI-MS spectra; computational details; frontier molecular orbital analysis; EPR spectra, NMR spectra,

https://doi.org/10.1021/jacs.3c02458
J. Am. Chem. Soc. XXXX, XXX, XXX−XXX

absorption spectra, and STEM images are provided (PDF)

Accession Codes

CCDC 2217282−2217283 contain the supplementary crystallographic data for this paper. These data can be obtained free of charge via www.ccdc.cam.ac.uk/data_request/cif, or by emailing data_request@ccdc.cam.ac.uk, or by contacting The Cambridge Crystallographic Data Centre, 12 Union Road, Cambridge CB2 1EZ, UK; fax: +44 1223 336033.

AUTHOR INFORMATION

Corresponding Author

Jarad A. Mason − *Department of Chemistry & Chemical Biology, Harvard University, Cambridge, Massachusetts 02138, United States;* orcid.org/0000-0003-0328-7775; Email: mason@chemistry.harvard.edu

Authors

Yingwei Li − *Department of Chemistry & Chemical Biology, Harvard University, Cambridge, Massachusetts 02138, United States;* orcid.org/0000-0002-4813-6009

Hong Ki Kim − *Department of Chemistry & Chemical Biology, Harvard University, Cambridge, Massachusetts 02138, United States;* orcid.org/0000-0002-6115-384X

Ryan D. McGillicuddy − *Department of Chemistry & Chemical Biology, Harvard University, Cambridge, Massachusetts 02138, United States*

Shao-Liang Zheng − *Department of Chemistry & Chemical Biology, Harvard University, Cambridge, Massachusetts 02138, United States;* orcid.org/0000-0002-6432-9943

Kevin J. Anderton − *Department of Chemistry & Chemical Biology, Harvard University, Cambridge, Massachusetts 02138, United States*

Grant J. Stec − *Department of Chemistry & Chemical Biology, Harvard University, Cambridge, Massachusetts 02138, United States*

Jaehyeong Lee − *Department of Chemistry & Chemical Biology, Harvard University, Cambridge, Massachusetts 02138, United States*

Dongtao Cui − *Department of Chemistry & Chemical Biology, Harvard University, Cambridge, Massachusetts 02138, United States*

Complete contact information is available at: https://pubs.acs.org/10.1021/jacs.3c02458

Author Contributions

[§]Y.L., H.K.K., and R.D.M. contributed equally to this work.

Notes

The authors declare no competing financial interest.

ACKNOWLEDGMENTS

We thank Dr. Jules Gardener for taking scanning transmission electron microscopy images and Dr. John Grimes for assistance with electron paramagnetic resonance measurements. We thank Prof. Mu-Hyun Baik for helpful discussions. We acknowledge support from the Major Research Instrumentation (MRI) Program of the National Science Foundation under NSF award no. 2216066 for the X-ray facility. This work was performed in part at the Harvard University Center for Nanoscale Systems (CNS); a member of the National Nanotechnology Coordinated Infrastructure Network (NNCI), which is supported by the National Science Foundation under NSF award no. ECCS-2025158. This research was partially supported by the Arnold and Mabel Beckman Foundation through a Beckman Young Investigator grant awarded to J.A.M.

REFERENCES

(1) Sankar, M.; He, Q.; Engel, R. V.; Sainna, M. A.; Logsdail, A. J.; Roldan, A.; Willock, D. J.; Agarwal, N.; Kiely, C. J.; Hutchings, G. J. Role of the Support in Gold-Containing Nanoparticles as Heterogeneous Catalysts. *Chem. Rev.* **2020**, *120*, 3890−3938.

(2) van Deelen, T. W.; Mejía, C. H.; de Jong, K. P. Control of Metal-Support Interactions in Heterogeneous Catalysts to Enhance Activity and Selectivity. *Nat. Catal.* **2019**, *2*, 955−970.

(3) Zhang, H.; Jin, M.; Xiong, Y.; Lim, B.; Xia, Y. Shape-Controlled Synthesis of Pd Nanocrystals and Their Catalytic Applications. *Acc. Chem. Res.* **2013**, *46*, 1783−1794.

(4) Xie, C.; Niu, Z.; Kim, D.; Li, M.; Yang, P. Surface and Interface Control in Nanoparticle Catalysis. *Chem. Rev.* **2020**, *120*, 1184−1249.

(5) Crespo-Quesada, M.; Yarulin, A.; Jin, M.; Xia, Y.; Kiwi-Minsker, L. Structure Sensitivity of Alkynol Hydrogenation on Shape- and Size-Controlled Palladium Nanocrystals: Which Sites Are Most Active and Selective? *J. Am. Chem. Soc.* **2011**, *133*, 12787−12794.

(6) Mahmoud, M. A.; Narayanan, R.; El-Sayed, M. A. Enhancing Colloidal Metallic Nanocatalysis: Sharp Edges and Corners for Solid Nanoparticles and Cage Effect for Hollow Ones. *Acc. Chem. Res.* **2013**, *46*, 1795−1805.

(7) Wang, A.; Li, J.; Zhang, T. Heterogeneous Single-Atom Catalysis. *Nat. Rev. Chem.* **2018**, *2*, 65−81.

(8) Li, Z.; Ji, S.; Liu, Y.; Cao, X.; Tian, S.; Chen, Y.; Niu, Z.; Li, Y. Well-Defined Materials for Heterogeneous Catalysis: From Nanoparticles to Isolated Single-Atom Sites. *Chem. Rev.* **2020**, *120*, 623−682.

(9) Jarupatrakorn, J.; Tilley, T. D. Silica-Supported, Single-Site Titanium Catalysts for Olefin Epoxidation. A Molecular Precursor Strategy for Control of Catalyst Structure. *J. Am. Chem. Soc.* **2002**, *124*, 8380−8388.

(10) Abbet, S.; Heiz, U.; Häkkinen, H.; Landman, U. CO Oxidation on a Single Pd Atom Supported on Magnesia. *Phys. Rev. Lett.* **2001**, *86*, 5950.

(11) Thomas, J. M.; Raja, R.; Lewis, D. W. Single-Site Heterogeneous Catalysts. *Angew. Chem., Int. Ed.* **2005**, *44*, 6456−6482.

(12) Flytzani-Stephanopoulos, M.; Gates, B. C. Atomically Dispersed Supported Metal Catalysts. *Annu. Rev. Chem. Biomol. Eng.* **2012**, *3*, 545−574.

(13) Jin, R.; Li, G.; Sharma, S.; Li, Y.; Du, X. Toward Active-Site Tailoring in Heterogeneous Catalysis by Atomically Precise Metal Nanoclusters with Crystallographic Structures. *Chem. Rev.* **2021**, *121*, 567−648.

(14) Du, Y.; Sheng, H.; Astruc, D.; Zhu, M. Atomically Precise Noble Metal Nanoclusters as Efficient Catalysts: A Bridge between Structure and Properties. *Chem. Rev.* **2020**, *120*, 526−622.

(15) Li, Y.; Li, S.; Nagarajan, A. V.; Liu, Z.; Nevins, S.; Song, Y.; Mpourmpakis, G.; Jin, R. Hydrogen Evolution Electrocatalyst Design: Turning Inert Gold into Active Catalyst by Atomically Precise Nanochemistry. *J. Am. Chem. Soc.* **2021**, *143*, 11102−11108.

(16) Li, Y.; Jin, R. Seeing Ligands on Nanoclusters and in Their Assemblies by X-Ray Crystallography: Atomically Precise Nanochemistry and Beyond. *J. Am. Chem. Soc.* **2020**, *142*, 13627−13644.

(17) Zhou, M.; Higaki, T.; Li, Y.; Zeng, C.; Li, Q.; Sfeir, M. Y.; Jin, R. Three-Stage Evolution from Nonscalable to Scalable Optical Properties of Thiolate-Protected Gold Nanoclusters. *J. Am. Chem. Soc.* **2019**, *141*, 19754−19764.

(18) Li, Y.; Cowan, M. J.; Zhou, M.; Luo, T.-Y.; Song, Y.; Wang, H.; Rosi, N. L.; Mpourmpakis, G.; Jin, R. Atom-by-Atom Evolution of the Same Ligand-Protected Au_{21}, Au_{22}, $Au_{22}Cd_1$, and Au_{24} Nanocluster Series. *J. Am. Chem. Soc.* **2020**, *142*, 20426−20433.

(19) Higaki, T.; Li, Y.; Zhao, S.; Li, Q.; Li, S.; Du, X.-S.; Yang, S.; Chai, J.; Jin, R. Atomically Tailored Gold Nanoclusters for Catalytic Application. *Angew. Chem., Int. Ed.* **2019**, *58*, 8291−8302.
(20) Li, Y.; Luo, T.-Y.; Zhou, M.; Song, Y.; Rosi, N. L.; Jin, R. A Correlated Series of Au/Ag Nanoclusters Revealing the Evolutionary Patterns of Asymmetric Ag Doping. *J. Am. Chem. Soc.* **2018**, *140*, 14235−14243.
(21) Li, G.; Sui, X.; Cai, X.; Hu, W.; Liu, X.; Chen, M.; Zhu, Y. Precisely Constructed Silver Active Sites in Gold Nanoclusters for Chemical Fixation of CO_2. *Angew. Chem., Int. Ed.* **2021**, *60*, 10573−10576.
(22) Kang, X.; Li, Y.; Zhu, M.; Jin, R. Atomically Precise Alloy Nanoclusters: Syntheses, Structures, and Properties. *Chem. Soc. Rev.* **2020**, *49*, 6443−6514.
(23) Wan, X.-K.; Wang, J.-Q.; Nan, Z.-A.; Wang, Q.-M. Ligand Effects in Catalysis by Atomically Precise Gold Nanoclusters. *Sci. Adv.* **2017**, *3*, e1701823.
(24) Zhang, B.; Chen, J.; Cao, Y.; Chai, O. J. H.; Xie, J. Ligand Design in Ligand-Protected Gold Nanoclusters. *Small* **2021**, *17*, 2004381.
(25) Li, G.; Jin, R. Gold Nanocluster-Catalyzed Semihydrogenation: A Unique Activation Pathway for Terminal Alkynes. *J. Am. Chem. Soc.* **2014**, *136*, 11347−11354.
(26) Wu, Z.; Jiang, D.; Mann, A. K. P.; Mullins, D. R.; Qiao, Z.-A.; Allard, L. F.; Zeng, C.; Jin, R.; Overbury, S. H. Thiolate Ligands as a Double-Edged Sword for CO Oxidation on CeO_2 Supported $Au_{25}(SCH_2CH_2Ph)_{18}$ Nanoclusters. *J. Am. Chem. Soc.* **2014**, *136*, 6111−6122.
(27) Li, Y.; Chen, Y.; House, S. D.; Zhao, S.; Wahab, Z.; Yang, J. C.; Jin, R. Interface Engineering of Gold Nanoclusters for CO Oxidation Catalysis. *ACS Appl. Mater. Interfaces* **2018**, *10*, 29425−29434.
(28) Kwak, K.; Choi, W.; Tang, Q.; Kim, M.; Lee, Y.; Jiang, D.; Lee, D. A Molecule-Like $PtAu_{24}(SC_6H_{13})_{18}$ Nanocluster as An Electrocatalyst for Hydrogen Production. *Nat. Commun.* **2017**, *8*, 14723.
(29) Gao, Z.-H.; Wei, K.; Wu, T.; Dong, J.; Jiang, D.; Sun, S.; Wang, L.-S. A Heteroleptic Gold Hydride Nanocluster for Efficient and Selective Electrocatalytic Reduction of CO_2 to CO. *J. Am. Chem. Soc.* **2022**, *144*, 5258−5262.
(30) Kulkarni, V. K.; Khiarak, B. N.; Takano, S.; Malola, S.; Albright, E. L.; Levchenko, T. I.; Aloisio, M. D.; Dinh, C.-T.; Tsukuda, T.; Häkkinen, H.; Crudden, C. M. N-Heterocyclic Carbene-Stabilized Hydrido Au_{24} Nanoclusters: Synthesis, Structure, and Electrocatalytic Reduction of CO_2. *J. Am. Chem. Soc.* **2022**, *144*, 9000−9006.
(31) Lin, Z.; Kanters, R. P. F.; Mingos, D. M. P. Closed-Shell Electronic Requirements for Condensed Clusters of the Group 11 Elements. *Inorg. Chem.* **1991**, *30*, 91−95.
(32) Walter, M.; Akola, J.; Lopez-Acevedo, O.; Jadzinsky, P. D.; Calero, G.; Ackerson, C. J.; Whetten, R. L.; Grönbeck, H.; Häkkinen, H. A Unified View of Ligand-Protected Gold Clusters as Superatom Complexes. *Proc. Natl. Acad. Sci. U.S.A.* **2008**, *105*, 9157−9162.
(33) Harkness, K. M.; Tang, Y.; Dass, A.; Pan, J.; Kothalawala, N.; Reddy, V. J.; Cliffel, D. E.; Demeler, B.; Stellacci, F.; Bakr, O. M.; McLean, J. A. $Ag_{44}(SR)_{30}^{4-}$: A Silver-Thiolate Superatom Complex. *Nanoscale* **2012**, *4*, 4269−4274.
(34) Narouz, M. R.; Takano, S.; Lummis, P. A.; Levchenko, T. I.; Nazemi, A.; Kaappa, S.; Malola, S.; Yousefalizadeh, G.; Calhoun, L. A.; Stamplecoskie, K. G.; Häkkinen, H.; Tsukuda, T.; Crudden, C. M. Robust, Highly Luminescent Au_{13} Superatoms Protected by N-Heterocyclic Carbenes. *J. Am. Chem. Soc.* **2019**, *141*, 14997−15002.
(35) Xu, W. W.; Zeng, X. C.; Gao, Y. Application of Electronic Counting Rules for Ligand-Protected Gold Nanoclusters. *Acc. Chem. Res.* **2018**, *51*, 2739−2747.
(36) Pei, Y.; Wang, P.; Ma, Z.; Xiong, L. Growth-Rule-Guided Structural Exploration of Thiolate-Protected Gold Nanoclusters. *Acc. Chem. Res.* **2019**, *52*, 23−33.
(37) Zeng, C.; Chen, Y.; Kirschbaum, K.; Appavoo, K.; Sfeir, M. Y.; Jin, R. Structural Patterns at All Scales in a Nonmetallic Chiral $Au_{133}(SR)_{52}$ Nanoparticle. *Sci. Adv.* **2015**, *1*, e1500045.
(38) Zhu, M.; Aikens, C. M.; Hendrich, M. P.; Gupta, R.; Qian, H.; Schatz, G. C.; Jin, R. Reversible Switching of Magnetism in Thiolate-Protected Au_{25} Superatoms. *J. Am. Chem. Soc.* **2009**, *131*, 2490−2492.
(39) Yan, J.; Malola, S.; Hu, C.; Peng, J.; Dittrich, B.; Teo, B. K.; Häkkinen, H.; Zheng, L.; Zheng, N. Co-Crystallization of Atomically Precise Metal Nanoparticles Driven by Magic Atomic and Electronic Shells. *Nat. Commun.* **2018**, *9*, 3357.
(40) Li, J.-J.; Liu, Z.; Guan, Z.-J.; Han, X.-S.; Shi, W.-Q.; Wang, Q.-M. A 59-Electron Non-Magic-Number Gold Nanocluster $Au_{99}(C{\equiv}CR)_{40}$ Showing Unexpectedly High Stability. *J. Am. Chem. Soc.* **2022**, *144*, 690−694.
(41) Wang, J.; Wang, Z.-Y.; Li, S.-J.; Zang, S.-Q.; Mak, T. C. W. Carboranealkynyl-Protected Gold Nanoclusters: Size Conversion and UV/Vis−NIR Optical Properties. *Angew. Chem., Int. Ed.* **2021**, *60*, 5959−5964.
(42) Kökçam-Demir, Ü.; Goldman, A.; Esrafili, L.; Gharib, M.; Morsali, A.; Weingart, O.; Janiak, C. Coordinatively Unsaturated Metal Sites (Open Metal Sites) in Metal−Organic Frameworks: Design and Applications. *Chem. Soc. Rev.* **2020**, *49*, 2751−2798.
(43) Lopez-Sanchez, J. A.; Dimitratos, N.; Hammond, C.; Brett, G. L.; Kesavan, L.; White, S.; Miedziak, P.; Tiruvalam, R.; Jenkins, R. L.; Carley, A. F.; Knight, D.; Kiely, C. J.; Hutchings, G. J. Facile Removal of Stabilizer-Ligands from Supported Gold Nanoparticles. *Nat. Chem.* **2011**, *3*, 551−556.
(44) Wan, X.-K.; Guan, Z.-J.; Wang, Q.-M. Homoleptic Alkynyl-Protected Gold Nanoclusters: $Au_{44}(PhC{\equiv}C)_{28}$ and $Au_{36}(PhC{\equiv}C)_{24}$. *Angew. Chem., Int. Ed.* **2017**, *56*, 11494−11497.
(45) Lei, Z.; Wan, X.-K.; Yuan, S.-F.; Guan, Z.-J.; Wang, Q.-M. Alkynyl Approach toward the Protection of Metal Nanoclusters. *Acc. Chem. Res.* **2018**, *51*, 2465−2474.
(46) Li, J.-J.; Guan, Z.-J.; Lei, Z.; Hu, F.; Wang, Q.-M. Same Magic Number but Different Arrangement: Alkynyl-Protected Au_{25} with D_3 Symmetry. *Angew. Chem., Int. Ed.* **2019**, *58*, 1083−1087.
(47) Hu, F.; Guan, Z.-J.; Yang, G.; Wang, J.-Q.; Li, J.-J.; Yuan, S.-F.; Liang, G.-J.; Wang, Q.-M. Molecular Gold Nanocluster Au156 Showing Metallic Electron Dynamics. *J. Am. Chem. Soc.* **2021**, *143*, 17059−17067.
(48) Wang, J.-Q.; Shi, S.; He, R.-L.; Yuan, S.-F.; Yang, G.-Y.; Liang, G.-J.; Wang, Q.-M. Total Structure Determination of the Largest Alkynyl-Protected Fcc Gold Nanocluster Au_{110} and the Study on Its Ultrafast Excited-State Dynamics. *J. Am. Chem. Soc.* **2020**, *142*, 18086−18092.
(49) Maity, P.; Tsunoyama, H.; Yamauchi, M.; Xie, S.; Tsukuda, T. Organogold Clusters Protected by Phenylacetylene. *J. Am. Chem. Soc.* **2011**, *133*, 20123−20125.
(50) Negishi, Y.; Nobusada, K.; Tsukuda, T. Glutathione-Protected Gold Clusters Revisited: Bridging the Gap between Gold(I)-Thiolate Complexes and Thiolate-Protected Gold Nanocrystals. *J. Am. Chem. Soc.* **2005**, *127*, 5261−5270.
(51) Guan, Z.-J.; Hu, F.; Li, J.-J.; Wen, Z.-R.; Lin, Y.-M.; Wang, Q.-M. Isomerization in Alkynyl-Protected Gold Nanoclusters. *J. Am. Chem. Soc.* **2020**, *142*, 2995−3001.
(52) Dong, H.; Liao, L.; Wu, Z. Two-Way Transformation between Fcc- and Nonfcc-Structured Gold Nanoclusters. *J. Phys. Chem. Lett.* **2017**, *8*, 5338−5343.
(53) Lei, Z.; Li, J.-J.; Wan, X.-K.; Zhang, W.-H.; Wang, Q.-M. Isolation and Total Structure Determination of an All Aklynyl-Protected Gold Nanocluster Au_{144}. *Angew. Chem., Int. Ed.* **2018**, *57*, 8639−8643.
(54) Li, Y.; Zhou, M.; Jin, R. Programmable Metal Nanoclusters with Atomic Precision. *Adv. Mater.* **2021**, *33*, 2006591.
(55) Wan, X.-K.; Wang, J.-Q.; Wang, Q.-M. Ligand-Protected Au_{55} with a Novel Structure and Remarkable CO_2 Electroreduction Performance. *Angew. Chem., Int. Ed.* **2021**, *60*, 20748−20753.
(56) Li, Y.; Higaki, T.; Du, X.; Jin, R. Chirality and Surface Bonding Correlation in Atomically Precise Metal Nanoclusters. *Adv. Mater.* **2020**, *32*, 1905488.

https://doi.org/10.1021/jacs.3c02458
J. Am. Chem. Soc. XXXX, XXX, XXX−XXX

(57) Sugiuchi, M.; Shichibu, Y.; Konishi, K. An Inherently Chiral Au_{24} Framework with Double-Helical Hexagold Strands. *Angew. Chem., Int. Ed.* **2018**, *57*, 7855−7859.
(58) Wang, Y.; Su, H.; Xu, C.; Li, G.; Gell, L.; Lin, S.; Tang, Z.; Häkkinen, H.; Zheng, N. An Intermetallic $Au_{24}Ag_{20}$ Superatom Nanocluster Stabilized by Labile Ligands. *J. Am. Chem. Soc.* **2015**, *137*, 4324−4327.
(59) Xu, J.; Xiong, L.; Cai, X.; Tang, S.; Tang, A.; Liu, X.; Pei, Y.; Zhu, Y. Evolution from Superatomic $Au_{24}Ag_{20}$ Monomers into Molecular-like $Au_{43}Ag_{38}$ Dimeric Nanoclusters. *Chem. Sci.* **2022**, *13*, 2778−2782.
(60) Yang, S.; Chai, J.; Song, Y.; Fan, J.; Chen, T.; Wang, S.; Yu, H.; Li, X.; Zhu, M. In Situ Two-Phase Ligand Exchange: A New Method for the Synthesis of Alloy Nanoclusters with Precise Atomic Structures. *J. Am. Chem. Soc.* **2017**, *139*, 5668−5671.
(61) Li, Y.; Zhou, M.; Song, Y.; Higaki, T.; Wang, H.; Jin, R. Double-Helical Assembly of Heterodimeric Nanoclusters into Supercrystals. *Nature* **2021**, *594*, 380−384.
(62) Tang, Y.; Sun, F.; Ma, X.; Qin, L.; Ma, G.; Tang, Q.; Tang, Z. Alkynyl and Halogen Co-Protected $(AuAg)_{44}$ Nanoclusters: A Comparative Study on Their Optical Absorbance, Structure, and Hydrogen Evolution Performance. *Dalton Trans.* **2022**, *51*, 7845−7850.
(63) Shen, H.; Mizuta, T. An Atomically Precise Alkynyl-Protected $PtAg_{42}$ Superatom Nanocluster and Its Structural Implications. *Chem. Asian J.* **2017**, *12*, 2904−2907.
(64) Kurashige, W.; Yamaguchi, M.; Nobusada, K.; Negishi, Y. Ligand-Induced Stability of Gold Nanoclusters Thiolate versus Selenolate. *J. Phys. Chem. Lett.* **2012**, *3*, 2649−2652.
(65) Kong, X. Y.; Wang, Z. L. Spontaneous Polarization-Induced Nanohelixes, Nanosprings, and Nanorings of Piezoelectric Nanobelts. *Nano Lett.* **2003**, *3*, 1625−1631.
(66) Gülseren, O.; Ercolessi, F.; Tosatti, E. Noncrystalline Structures of Ultrathin Unsupported Nanowires. *Phys. Rev. Lett.* **1998**, *80*, 3775−3778.
(67) Kondo, Y.; Takayanagi, K. Synthesis and Characterization of Helical Multi-Shell Gold Nanowires. *Science* **2000**, *289*, 606−608.
(68) Cho, K.-S.; Talapin, D. V.; Gaschler, W.; Murray, C. B. Designing PbSe Nanowires and Nanorings through Oriented Attachement of Nanoparticles. *J. Am. Chem. Soc.* **2005**, *127*, 7140−7147.
(69) Li, Y.; Jin, R. Magnetism of Atomically Precise Gold and Doped Nanoclusters: Delocalized Spin and Interparticle Coupling. *J. Phys. Chem. C* **2021**, *125*, 15773−15784.
(70) Antonello, S.; Perera, N. V.; Ruzzi, M.; Gascón, J. A.; Maran, F. Interplay of Charge State, Lability, and Magnetism in the Molecule-like $Au_{25}(SR)_{18}$ Cluster. *J. Am. Chem. Soc.* **2013**, *135*, 15585−15594.
(71) Tofanelli, M. A.; Salorinne, K.; Ni, T. W.; Malola, S.; Newell, B.; Phillips, B.; Häkkinen, H.; Ackerson, C. J. Jahn-Teller Effects in $Au_{25}(SR)_{18}$. *Chem. Sci.* **2016**, *7*, 1882−1890.
(72) Li, Y.; Biswas, S.; Luo, T.-Y.; Juarez-Mosqueda, R.; Taylor, M. G.; Mpourmpakis, G.; Rosi, N. L.; Hendrich, M. P.; Jin, R. Doping Effect on the Magnetism of Thiolate-Capped 25-Atom Alloy Nanoclusters. *Chem. Mater.* **2020**, *32*, 9238−9244.
(73) Xie, S.; Tsunoyama, H.; Kurashige, W.; Negishi, Y.; Tsukuda, T. Enhancement in Aerobic Alcohol Oxidation Catalysis of Au25 Clusters by Single Pd Atom Doping. *ACS Catal.* **2012**, *2*, 1519−1523.
(74) Yoskamtorn, T.; Yamazoe, S.; Takahata, R.; Nishigaki, J.; Thivasasith, A.; Limtrakul, J.; Tsukuda, T. Thiolate-Mediated Selectivity Control in Aerobic Alcohol Oxidation by Porous Carbon-Supported Au25 Clusters. *ACS Catal.* **2014**, *4*, 3696−3700.
(75) Adnan, R. H.; Golovko, V. B. Benzyl Alcohol Oxidation Using Gold Catalysts Derived from Au_8 Clusters on TiO_2. *Catal. Lett.* **2019**, *149*, 449−455.
(76) Fang, J.; Li, J.; Zhang, B.; Yuan, X.; Asakura, H.; Tanaka, T.; Teramura, K.; Xie, J.; Yan, N. The Support Effect on the Size and Catalytic Activity of Thiolated Au_{25} Nanoclusters as Precatalysts. *Nanoscale* **2015**, *7*, 6325−6333.
(77) Liu, Y.; Tsunoyama, H.; Akita, T.; Tsukuda, T. Efficient and Selective Epoxidation of Styrene with TBHP Catalyzed by Au_{25} Clusters on Hydroxyapatite. *Chem. Commun.* **2010**, *46*, 550−552.
(78) Zhang, B.; Kaziz, S.; Li, H.; Hevia, M. G.; Wodka, D.; Mazet, C.; Bürgi, T.; Barrabés, N. Modulation of Active Sites in Supported $Au_{38}(SC_2H_4Ph)_{24}$ Cluster Catalysts: Effect of Atmosphere and Support Material. *J. Phys. Chem. C* **2015**, *119*, 11193−11199.
(79) Zhang, B.; Fang, J.; Li, J.; Lau, J. J.; Mattia, D.; Zhong, Z.; Xie, J.; Yan, N. Soft, Oxidative Stripping of Alkyl Thiolate Ligands from Hydroxyapatite-Supported Gold Nanoclusters for Oxidation Reactions. *Chem. Asian J.* **2016**, *11*, 532−539.
(80) Zhu, Y.; Qian, H.; Jin, R. An Atomic-Level Strategy for Unraveling Gold Nanocatalysis from the Perspective of $Au_n(SR)_m$ Nanoclusters. *Chem. - Eur. J.* **2010**, *16*, 11455−11462.
(81) Yuan, S.-F.; Lei, Z.; Guan, Z.-J.; Wang, Q.-M. Atomically Precise Preorganization of Open Metal Sites on Gold Nanoclusters with High Catalytic Performance. *Angew. Chem., Int. Ed.* **2021**, *60*, 5225−5229.
(82) Falivene, L.; Credendino, R.; Poater, A.; Petta, A.; Serra, L.; Oliva, R.; Scarano, V.; Cavallo, L. SambVca 2. A Web Tool for Analyzing Catalytic Pockets with Topographic Steric Maps. *Organometallics* **2016**, *35*, 2286−2293.
(83) Falivene, L.; Cao, Z.; Petta, A.; Serra, L.; Poater, A.; Oliva, R.; Scarano, V.; Cavallo, L. Towards the Online Computer-Aided Design of Catalytic Pockets. *Nat. Chem.* **2019**, *11*, 872−879.
(84) Conte, M.; Miyamura, H.; Kobayashi, S.; Chechik, V. Spin Trapping of Au−H Intermediate in the Alcohol Oxidation by Supported and Unsupported Gold Catalysts. *J. Am. Chem. Soc.* **2009**, *131*, 7189−7196.
(85) Kumar, G.; Tibbitts, L.; Newell, J.; Panthi, B.; Mukhopadhyay, A.; Rioux, R. M.; Pursell, C. J.; Janik, M.; Chandler, B. D. Evaluating Differences in the Active-Site Electronics of Supported Au Nanoparticle Catalysts Using Hammett and DFT Studies. *Nat. Chem.* **2018**, *10*, 268−274.
(86) Takano, S.; Hirai, H.; Muramatsu, S.; Tsukuda, T. Hydride-Doped Gold Superatom $(Au_9H)^{2+}$: Synthesis, Structure, and Transformation. *J. Am. Chem. Soc.* **2018**, *140*, 8380−8383.
(87) Takano, S.; Ito, S.; Tsukuda, T. Efficient and Selective Conversion of Phosphine-Protected $(MAu_8)^{2+}$ (M = Pd, Pt) Superatoms to Thiolate-Protected $(MAu_{12})^{6+}$ or Alkynyl-Protected $(MAu_{12})^{4+}$ Superatoms via Hydride Doping. *J. Am. Chem. Soc.* **2019**, *141*, 15994−16002.
(88) Hu, G.; Tang, Q.; Lee, D.; Wu, Z.; Jiang, D. Metallic Hydrogen in Atomically Precise Gold Nanoclusters. *Chem. Mater.* **2017**, *29*, 4840−4847.
(89) Yuan, X.; Sun, C.; Li, X.; Malola, S.; Teo, B. K.; Häkkinen, H.; Zheng, L.-S.; Zheng, N. Combinatorial Identification of Hydrides in a Ligated Ag_{40} Nanocluster with Noncompact Metal Core. *J. Am. Chem. Soc.* **2019**, *141*, 11905−11911.
(90) Zeng, C.; Chen, Y.; Iida, K.; Nobusada, K.; Kirschbaum, K.; Lambright, K. J.; Jin, R. Gold Quantum Boxes: On the Periodicities and the Quantum Confinement in the Au_{28}, Au_{36}, Au_{44}, and Au_{52} Magic Series. *J. Am. Chem. Soc.* **2016**, *138*, 3950−3953.
(91) Li, Y.; Song, Y.; Zhang, X.; Liu, T.; Xu, T.; Wang, H.; Jiang, D.; Jin, R. Atomically Precise Au_{42} Nanorods with Longitudinal Excitons for an Intense Photothermal Effect. *J. Am. Chem. Soc.* **2022**, *144*, 12381−12389.

https://doi.org/10.1021/jacs.3c02458
J. Am. Chem. Soc. XXXX, XXX, XXX−XXX